

# A 0.18-V 382- $\mu$ W Bluetooth Low-Energy Receiver Front-End With 1.33-nW Sleep Power for Energy-Harvesting Applications in 28-nm CMOS

Haidong Yi, *Student Member, IEEE*, Wei-Han Yu, *Student Member, IEEE*, Pui-In Mak<sup>ID</sup>, *Senior Member, IEEE*, Jun Yin<sup>ID</sup>, *Member, IEEE*, and Rui P. Martins, *Fellow, IEEE*

**Abstract**—This paper describes an ultra-low-voltage Bluetooth low-energy (BLE) receiver (RX) front end with an on-chip micropower manager ( $\mu$ PM) to customize the internal voltage domains. It aims at direct powering by the sub-0.5-V energy-harvesting sources like the on-body thermoelectric, eliminating the loss and cost of the interim dc–dc converters. Specifically, the RX incorporates: 1) a two-stage power-gating low-noise amplifier with fully on-chip input-impedance matching and passive gain boosting reducing both the active and sleep power; 2) a class-D voltage-controlled oscillator (VCO) in parallel with a class-C starter to secure a fast startup; and 3) a  $\mu$ PM using ring-VCO-locked charge pumps and bandgap references to withstand the supply-voltage variation (0.18–0.3 V). Fabricated in 28-nm CMOS, the RX operates down to a 0.18-V supply, while exhibiting 11.3-dB NF and  $-12.5$ -dBm out-of-band IIP3. The VCO shows  $< -113$  dBc/Hz phase noise at 2.5-MHz offset. The active and sleep power are 382  $\mu$ W and 1.33 nW, respectively.

**Index Terms**—Bandgap reference (BGR), Bluetooth low energy (BLE), charge pump (CP), class-D voltage-controlled oscillator (VCO), CMOS, energy harvesting, low-noise amplifier (LNA), micropower manager ( $\mu$ PM), power-gating, receiver (RX), ultra-low power (ULP), ultra-low voltage (ULV).

## I. INTRODUCTION

FOR true mobility of Internet-of-Things (IoT) products, the relaxed specifications of Bluetooth low energy (BLE) [1] are in favor of direct powering by ambient energies, freeing the cost of routine battery replacement. Energy sources like the on-body thermoelectric [2] are promising, providing a power-generation density of  $\sim 50$   $\mu$ W/cm<sup>2</sup>, and a relatively stable output power comparing to other types of energy harvesters such as vibration. The key challenge hindering its utility is

Manuscript received November 10, 2017; revised January 18, 2018 and March 9, 2018; accepted March 9, 2018. Date of publication April 4, 2018; date of current version May 24, 2018. This paper was approved by Associate Editor Ichiro Fujimori. This work was supported in part by the University of Macau-MYRG2017-00223-AMSV, and in part by Macau Science and Technology Development Fund (FDCT)—SKL Fund. (*Corresponding author: Pui-In Mak.*)

H. Yi, W.-H. Yu, P.-I. Mak, and J. Yin are with the State-Key Laboratory of Analog and Mixed-Signal VLSI and the Faculty of Science and Technology, Department of Electrical and Computer Engineering, University of Macau, Macau 999078, China (e-mail: pimak@umac.mo).

R. P. Martins is with the State-Key Laboratory of Analog and Mixed-Signal VLSI and the Faculty of Science and Technology, Department of Electrical and Computer Engineering, University of Macau, Macau 999078, China, on leave from the Instituto Superior Técnico/Universidade de Lisboa, 1049-001 Lisbon, Portugal (e-mail: rmartins@umac.mo).

Color versions of one or more of the figures in this paper are available online at <http://ieeexplore.ieee.org>.

Digital Object Identifier 10.1109/JSSC.2018.2815987

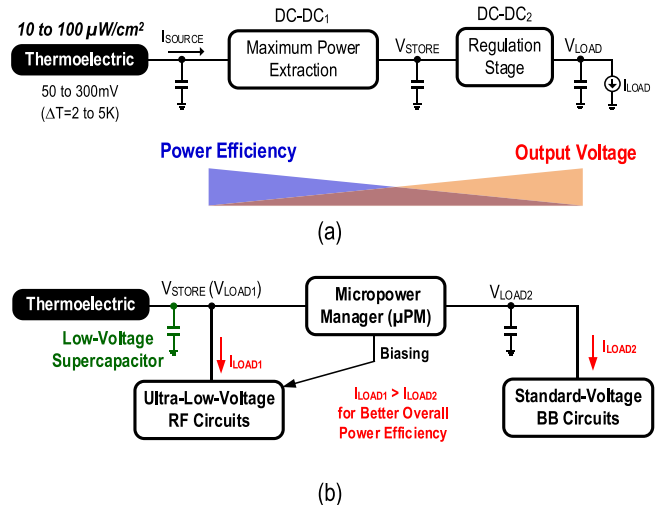


Fig. 1. (a) Conventional energy-harvesting topology. (b) Codesign between our proposed energy-harvesting topology and ULV RF circuits, where a  $\mu$ PM can provide the critical biases and support the standard voltage BB circuits.

the deeply low and inconstant output voltage (50–300 mV) [3]. The energy harvester is typically followed by one or more dc–dc converter(s) for maximum power extraction and regulation as depicted in Fig. 1(a) [3]. Yet, the conversion efficiency ( $\eta$ ) of most dc–dc converters is limited to 40%–75% [4], while entailing external bulky inductors and capacitors. Another issue is related to the voltage-boosting factor that has to sacrifice the output current, as shown in Fig. 1(a), where  $I_{SOURCE} = I_{LOAD} \times \text{voltage-boosting factor} \times 1/\eta$ . If the voltage-boosting factor is 5 (0.2 V  $\rightarrow$  1 V) and  $\eta = 75\%$  for the dc–dc converter, only 15% of  $I_{SOURCE}$  finally goes as  $I_{LOAD}$ .

Current-reuse receivers (RXs) are getting popular for ultra-low-power (ULP) radios. Transistor stacking in sub-1-V CMOS technologies, regrettably, reduces both the voltage headroom and block-to-block isolation. In [5], merging the voltage-controlled oscillator (VCO) with the low-noise amplifier (LNA) and mixers allows significant power savings, but the VCO may be pulled by the RF blockers, and the noises of the RX path and LO path (VCO) will cross-affect each other. Although the VCO pulling and noise crosstalk can be prevented by separately powering the current-reuse RX path and LO path [6], the cost and power loss of the extra dc–dc converter are unneglectable.

Alternatively, the sub-0.5-V energy-harvesting sources favor the use of an ultra-low-voltage (ULV) supply to build an ULP radio. In [7], the supply voltage ( $V_{DD}$ ) is minimized to 0.3 V by extensively applying inductor-based RF circuits to maximize the voltage headroom, and forward-body-biasing to reduce the transistor's threshold voltage ( $V_{TH}$ ) while raising their intrinsic  $f_T$ . Yet, the tradeoff is a substantial increase of the transistor's leakage current (e.g., Fig. 2(b) [7]), that is unbearable for low-duty-cycle IoT applications [8] since the BLE RX stays mostly ( $\sim 99\%$ ) in the sleep mode.

The presented RX [9] innovates an on-chip micropower manager ( $\mu\text{PM}$ ) to enable ULV and ULP operations [Fig. 1(b)]. The RF circuits (LNA and VCO) are ULV-enabled to directly draw dc current ( $I_{LOAD1}$ ) from the energy-harvesting source ( $V_{LOAD1}$ ), avoiding any interim power converters.  $V_{LOAD1}$  can be stabilized by a thin-film low-voltage supercapacitor [10], which also serves as the energy reservoir. Its capacitance is subject to the required duty-cycle ratio. Only the ULP baseband (BB) circuits entail a higher standard voltage ( $V_{LOAD2}$ ) that can be customized via the  $\mu\text{PM}$ -RX codesign. Keeping  $I_{LOAD2}$  in the level of hundreds of  $\mu\text{A}$  benefits the design of the  $\mu\text{PM}$ , as it can be built by fully on-chip switched-capacitor charge pumps (CPs) for voltage boosting (i.e., no external bulky inductors or capacitors). Also, since most RF performances such as noise figure (NF), small-signal gain, and input-impedance matching are related to the supply current rather than the supply voltage, ULP Bandgap references (BGRs) can be incorporated in the  $\mu\text{PM}$  to bias the RF circuits against process-voltage-temperature (PVT) variations. The tolerability of RF blockers can be addressed via properly designing the LNA with gain control according to the sensitivity target. Other key features of the  $\mu\text{PM}$  are capable of self-startup down to 0.15 V, and regulated output voltages against supply-voltage variation to reduce the excessive power.

This paper is organized as follows. Section II overviews the RX system architecture. The  $\mu\text{PM}$  is detailed in Section III, followed by the designs of the VCO and RX-path building blocks in Sections IV and V, respectively. Section VI summarizes and discusses the measurement results, and finally the conclusions are drawn in Section VII.

## II. SYSTEM OVERVIEW

The presented ULV RX front-end (Fig. 2) is headed by a single-ended LNA with on-chip input-impedance matching. It is followed by a passive  $RC$ - $CR$  network for I/Q generation ( $V_{rfI}$ ,  $V_{rfQ}$ ), and four passive mixers for frequency down-conversion and single-to-differential conversion. The local oscillator (LO) signals are the differential outputs ( $V_{osc\pm}$ ) of a switching-type Class-D VCO [11] that features output-swing enhancement to improve the mixer's NF and conversion gain, while preventing the need of power-hungry LO buffers. The obtained four-phase BB signals (I/Q and differential) are then amplified by four BB transimpedance amplifiers (TIAs), and finally buffered off-chip for 50- $\Omega$  measurements ( $V_{out,I\pm}$ ,  $V_{out,Q\pm}$ ). The noncascoded inductor-based LNA and VCO are ULV-enabled to operate against an uncertain energy-harvesting voltage ( $V_{DD,EH} \approx 0.15$ –0.30 V). The critical biases of the

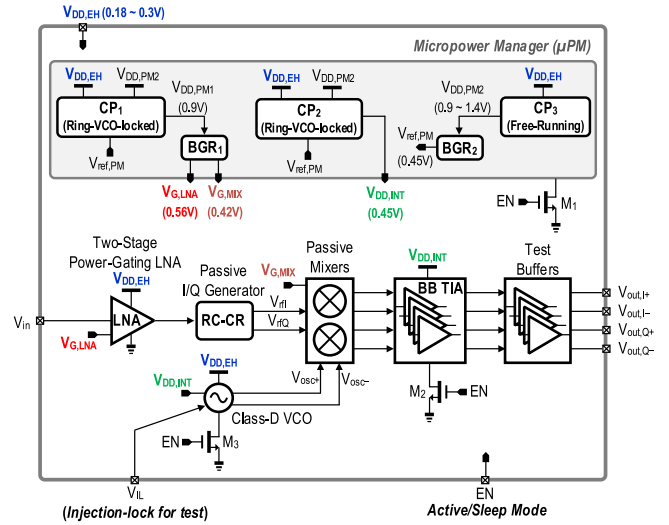


Fig. 2. System overview of the proposed ULV RX front end with an on-chip  $\mu\text{PM}$  to customize the internal supply and biases. The power-hungry LNA and VCO are ULV-enabled to directly draw current from  $V_{DD,EH}$ .  $V_{IL}$  is for injection locking the VCO during the RX measurements as there is no PLL.

LNA ( $V_{G,LNA}$ ) and mixers ( $V_{G,MIX}$ ), as well as the internal supply ( $V_{DD,INT}$ ) of the BB TIAs, are generated by the  $\mu\text{PM}$ . Inside the  $\mu\text{PM}$ , there are three CPs ( $CP_{1,2,3}$ ) and two BGRs that will be detailed in Section III.  $CP_1$  is designed to offer a  $\sim 0.9$ -V supply, with a small current budget, for BGR<sub>1</sub> that generates  $V_{G,LNA}$  and  $V_{G,MIX}$ , securing the robustness of the LNA and mixers against PVT variations. BGR<sub>1</sub> inherently rejects the output ripple of  $CP_1$ . For  $CP_2$ , it is designed to generate a  $\sim 450$ -mV  $V_{DD,INT}$ , with a relatively higher current budget ( $\sim 100 \mu\text{A}$ ), to power up the four BB TIAs, and bias the Class-C starter of the VCO to be detailed in Section IV.  $CP_2$  features a set of interleaved clocks for output-ripple reduction, minimizing such ripple noise from corrupting the BB TIAs.  $CP_3$  is a free-running design to secure a fast self-startup. It activates BGR<sub>2</sub> to generate an essential reference voltage ( $V_{ref,PM}$ ) for the feedback control of  $CP_{1,2}$ ; both feature a ring-VCO-locked loop to regulate their outputs ( $V_{DD,PM1}$  and  $V_{DD,INT}$ ) against  $V_{DD,EH}$  variation.

In the sleep mode, high- $V_{TH}$  (HVT) power-gating NMOS transistors ( $M_{1-3}$ ) are incorporated for sleep-current suppression of the  $\mu\text{PM}$ , BB TIAs, and VCO. The LNA features a self-shutdown mechanism to avoid NF and linearity penalties due to the extra power-gating switches, to be detailed in Section V.

## III. MICROPOWER MANAGER ( $\mu\text{PM}$ )

The  $\mu\text{PM}$  aims to withstand a  $V_{DD,EH}$  range from 0.15 to 0.3 V. The total power budget is  $\sim 100 \mu\text{W}$ , and the design details of  $CP_{1-3}$  are presented next.

### A. $CP_{1-3}$ Driven by Bootstrapped Ring-VCO (BTRO)

The aimed  $V_{DD,EH}$  is as low as 0.15 V, while the standard analog blocks like the BGRs should operate at a voltage of  $\sim 0.9$  V. Thus,  $CP_1$  is designed with a  $10\times$  conversion

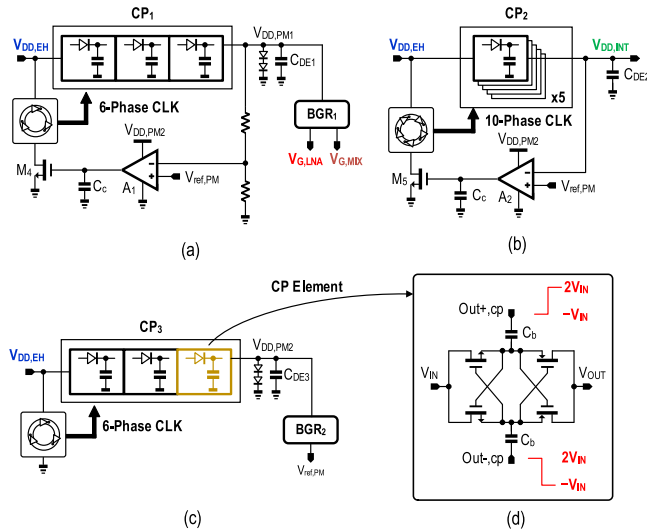


Fig. 3. (a) Ring-VCO-locked CP1. (b) Ring-VCO-locked CP2. (c) Free-running CP3 for self-startup. (d) Schematic of each CP element. The sketched swing of  $Out_{\pm, cp}$  is in the ideal case.

ratio using three sub-cells in series [Fig. 3(a)]. The six-phase clocks are generated by a three-stage differential bootstrapped ring-VCO (BTRO). Ideally, CP<sub>1</sub> delivers  $V_{DD, PM1} = V_{DD, EH} + 3V_{DD, EH} + 3V_{DD, EH} + 3V_{DD, EH} = 10V_{DD, EH}$ , that is 1.5 V at  $V_{DD, EH} = 0.15$  V.  $V_{DD, PM1}$  from CP<sub>1</sub> powers up BGR<sub>1</sub> that offers the gate biases of the LNA ( $V_{G, LNA}$ ) and mixers ( $V_{G, MIX}$ ).

Since the BB TIAs require a minimum 0.45-V  $V_{DD, INT}$  with a 100- $\mu$ A current budget, CP<sub>2</sub> is designed with a 4 $\times$  conversion ratio:  $V_{DD, INT} = V_{DD, EH} + 3V_{DD, EH} = 4V_{DD, EH}$ . There are five sub-cells in parallel to enhance the output current, as shown in Fig. 3(b). The 10-phase clocks are the intrinsic outputs of a five-stage differential BTRO without extra buffering.  $V_{DD, PM2}$  from CP<sub>3</sub> [Fig. 3(c)] powers up both BGR<sub>2</sub> to generate  $V_{ref, PM}$ , and the error amplifiers ( $A_{1,2}$ ) used for the feedback control, as shown in Fig. 3(a) and (b). CP<sub>3</sub> utilizes a free-running ring-VCO for self-startup. The cascode diodes at  $V_{DD, PM1}$  and  $V_{DD, PM2}$  are used to limit the maximum voltage below 1.4 V for overvoltage protection, and the BGRs use the 1.8-V-thick-oxide transistors to ensure the device reliability for the input supply range. The smoothing capacitors ( $C_{DE1-3}$ ) aid output-ripple reduction.

The CP elements of CP<sub>1-3</sub> are the same as that shown in Fig. 3(d), using a cross-coupled structure to boost the input voltage ( $V_{DD, EH}$ ) targeting a value as low as 0.15 V, with the device size computationally optimized for a maximum power conversion efficiency (PCE). The three- and five-stage differential BTROs are detailed in Fig. 4. The single-ended BTRO has been reported in [12], whereas the employed BTRO is based on differential bootstrapped inverters [13] that can ideally offer a clock swing up to  $3 \times V_{DD, EH}$  to drive up the CP elements. In practice, due to the conduction loss of the transistors and voltage drop on the boosting capacitors ( $C_b$ ) caused by the loading current, the clock swing is only  $\sim 2.3 \times V_{DD, EH} = 0.35 V_{pp}$  (simulation) in the employed 28-nm CMOS process, but is still adequate to operate the CP elements

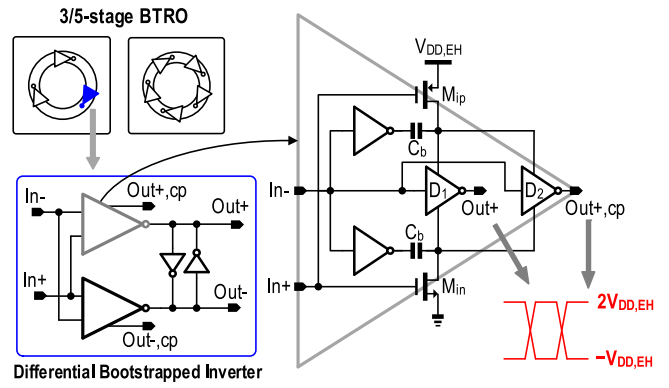


Fig. 4. 3/5-stage BTRO. The ideal output swing is  $3 \times V_{DD, EH}$ .  $Out_{\pm}$  is for driving the next inverter using D1, and  $Out_{\pm, cp}$  is for driving the CP elements using D2.

in the range of tens of MHz ( $\sim 20$  MHz at 0.15-V  $V_{DD, EH}$ ). Also, unlike the single-ended BTRO counterpart,  $M_{ip}$  and  $M_{in}$  here can be driven more synchronically by  $In+$ , instead of  $Out+$ , to reduce the power loss due to reverse current. The BTRO's outputs can also be separately out via the inverters D<sub>1</sub> and D<sub>2</sub>, to reduce the dependence of the oscillation frequency on the load drivability. The BTRO is designed with low-threshold-voltage ( $V_{TH} \approx 260$  mV) transistors. During the startup, the inverters inside each BTRO work in the sub-threshold region, but could ensure a loop gain of  $\sim 12$  dB at 0 $^\circ$  phase shift to ensure oscillation. The signal swing, when entering the steady state, will be boosted to  $3 \times V_{DD, EH}$  ( $-V_{DD, EH}$  to  $2V_{DD, EH}$ ), and the transistors will be driven into the triode region with the boosted swing to reduce the conduction loss.

The optimization of CP<sub>1-3</sub> is based on simple resistive loads ( $R_L$ ) in simulation. CP<sub>1,2,3</sub> are optimized at  $V_{DD, EH} = 0.15$  V. CP<sub>1</sub> has the same circuit parameters as CP<sub>3</sub> excluding the feedback loop.  $R_L$  of CP<sub>1</sub> is 500 k $\Omega$  to model the power consumption of BGR<sub>1</sub> and resistors in the voltage divider.  $R_L$  of CP<sub>2</sub> is 4.5 k $\Omega$  to model the power consumption of the BB TIAs ( $\sim 45$   $\mu$ W). With a 2.5-pF MOM capacitor  $C_b$ , a 41% PCE is obtained for CP<sub>1,3</sub>, and  $V_{DD, PM1,2}$  is 1.11 V. For CP<sub>2</sub>,  $C_b = 15$  pF and  $V_{DD, INT} = 0.48$  V lead to a 49% PCE, with the power consumption of the feedback circuits of CP<sub>1,2</sub> excluded from the PCE calculation. Although the PCE of CP<sub>1,3</sub> is lower than that of CP<sub>2</sub>, the power consumption of CP<sub>1,3</sub> is only  $\sim 5.93$   $\mu$ W, that is much smaller than that of CP<sub>2</sub> ( $\sim 96$   $\mu$ W). Hence, the PCE of the whole  $\mu$ PM is dominated by CP<sub>2</sub>.

### B. Ring-VCO-Locked Loop for Voltage Regulation

To tolerate an uncertain  $V_{DD, EH}$ , CP<sub>1,2</sub> are rounded by a ring-VCO-locked loop to regulate  $V_{DD, PM1}$  and  $V_{DD, INT}$ , and reduce the excessive power when  $V_{DD, EH}$  goes unnecessarily high. Especially for the BB TIAs (inverter-like amplifiers), their dc currents will raise nonlinearly with  $V_{DD, INT}$ . To surmount it,  $A_1$  ( $A_2$ ) are added to sense  $V_{DD, PM1}$  ( $V_{DD, INT}$ ) and return the control signal via the current source  $M_4$  ( $M_5$ ) for voltage regulation, as shown in Fig. 3(a) and (b). From PVT simulations, the feedback loop continues functioning when

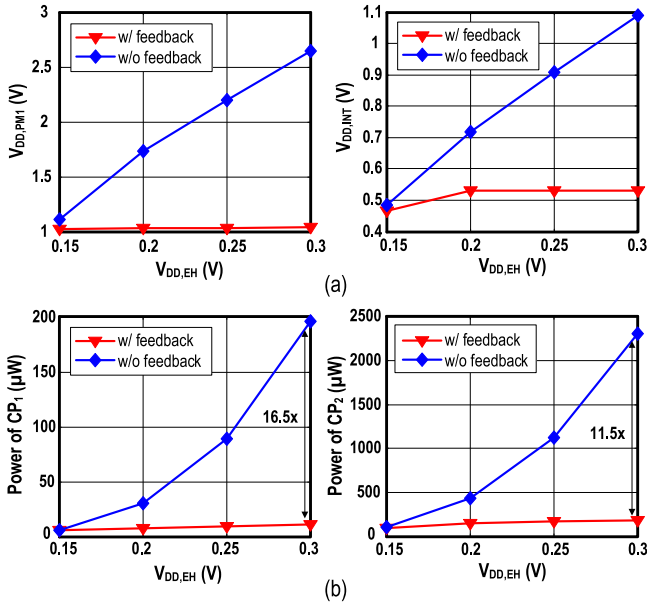


Fig. 5. Performances of CP1 (left) and CP2 (right) versus  $V_{DD,EH}$  with and without feedback control. (a) Output voltage. (b) Power consumption.

$V_{DD,EH}$  is down to 0.15 V. Considering the tradeoff between the stability and settling time of the two feedback loops, the compensation capacitors  $C_c$  in Fig. 3(a) and (b) are set at 3 pF.  $A_{1,2}$  have a simulated open loop gain of 35 dB, while consuming 0.27  $\mu$ W.

The simulated output voltage and power consumption of CP<sub>1, 2</sub> versus  $V_{DD,EH}$  with and without the feedback control are compared in Fig. 5(a) and (b), respectively. The variation of output voltage against  $V_{DD,EH}$  is  $\Delta V_{DD,PM1}(\Delta V_{DD,INT})/\Delta V_{DD,EH}$ . With the feedback control,  $V_{DD,PM1}$  is clipped to  $\sim 1.03$  V for  $V_{DD,EH} = 0.15\text{--}0.3$  V, corresponding to a sensitivity of 0.11 V/V.  $V_{DD,INT}$  is bounded to  $\sim 0.53$  V, but with a higher sensitivity of 0.45 V/V (due to the low output voltage at 0.15 V). Both results are considerable improved when comparing with no feedback, i.e., 10.2 V/V for  $V_{DD,PM1}$  and 4.06 V/V for  $V_{DD,INT}$ . Similarly, with feedback control, the power consumption of CP<sub>1</sub> (CP<sub>2</sub>) only mildly increases from 5.93 to 11.2  $\mu$ W (96–184  $\mu$ W) with the rising of  $V_{DD,EH}$ . Otherwise, it will jump to 196  $\mu$ W for CP<sub>1</sub> and 2.3 mW for CP<sub>2</sub>. From Fig. 5(b), we can derive that the total power consumption of CP<sub>1</sub> and CP<sub>2</sub> is controlled to be 195  $\mu$ W at  $V_{DD,EH} = 0.3$  V, saving the excessive power by  $\sim 11.8\times$  against no feedback.

### C. Output-Ripple Reduction of CP<sub>1</sub> and CP<sub>2</sub>

With  $C_{DE1} = 6$  pF for CP<sub>1</sub>, the simulated maximum output ripple of  $V_{DD,PM1}$  versus  $V_{DD,EH}$  is reduced to 3.44 mV when  $V_{DD,EH}$  increases. The ripple frequency is  $2\times$  of the BTRO's frequency ( $\sim 40$  MHz) at  $V_{DD,EH} = 0.15$  V. The simulated supply rejection of the BGR<sub>1,2</sub> is 35 dB at dc, and 9.5 dB at 40 MHz. Thus, the maximum ripple of  $V_{G,LNA}$  and  $V_{G,MIX}$  can be reduced to 1.13 mV.

In order to reduce the ripple of  $V_{DD,INT}$  while not using a large  $C_{DE2}$ , CP<sub>2</sub> can benefit from interleaved clocks. With

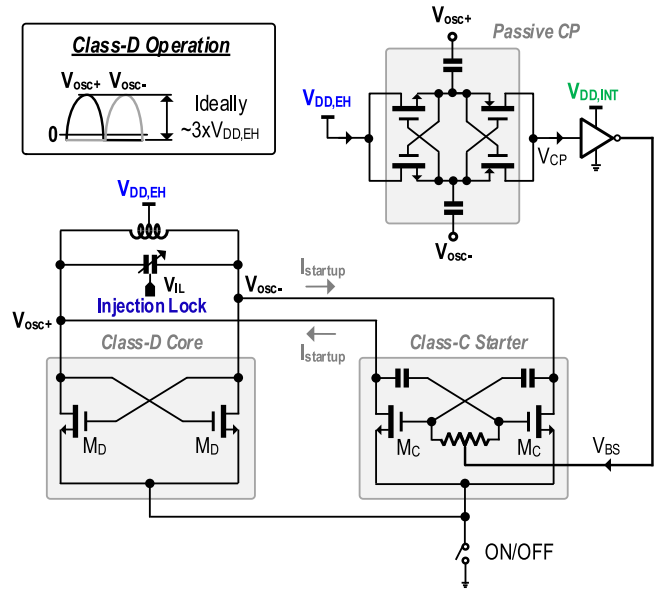


Fig. 6. ULV class-D VCO with a class-C starter to assist a fast startup. The passive CP senses the swing buildup at  $V_{osc\pm}$  to activate/deactivate the class-C starter before/after startup. The steady-state oscillation is governed by the class-D VCO.

10-phase clocks equally distributed to the five sub-cells of CP<sub>2</sub>, the output ripple is ideally reduced by  $5\times$  against two-phase clocks [14]–[16]. Thus, the interleaved clocks benefit the die area. The simulated maximum ripple of  $V_{DD,INT}$  is  $<0.77$  mV<sub>pp</sub> at an affordable  $C_{DE2}$  of 18.9 pF, which contributes to the overall NF degradation by  $<1$  dB at the RX's differential BB outputs.

## IV. ULV CLASS-D VCO WITH A CLASS-C STARTER

To maximize the power efficiency it is preferable that the VCO works directly at  $V_{DD,EH}$ . Since the outputs of the VCO will directly drive the mixers without any additional buffers, a large VCO output swing is favored to improve the RX NF and conversion gain. Here, a switching-type class-D topology (Fig. 6) is chosen since it ideally can generate an output swing close to  $\sim 3\times V_{DD,EH}$  by enlarging the cross-coupled transistors, and removing the current-biased circuitry of the conventional class-B VCO, which renders it suitable for ULV operation [11]. On the other hand, the oscillation frequency of the class-D VCO is sensitive to the supply pushing at an ULV  $V_{DD,EH}$ . Since the speed of supply variation caused by the environment change is quite slow when powered by an energy-harvesting source, a phase-locked loop (PLL) with a typical loop bandwidth of several hundreds of kHz should be fast enough to stabilize the VCO frequency when receiving the data.

Yet, the cross-coupled transistors may not offer adequate negative transconductance at ULV  $V_{DD,EH}$  in the presence of PVT variations, which would cause the VCO to fail to startup. Even using a large-size (400  $\mu$ m/28 nm) low- $V_T$  device for  $M_D$ , the simulated small-signal  $g_m$  is below the startup criteria when  $T < -10$   $^{\circ}$ C at slow corner and  $V_{DD,EH} = 0.18$  V [Fig. 7(a)]. To surmount this issue, a class-C starter (Fig. 6)

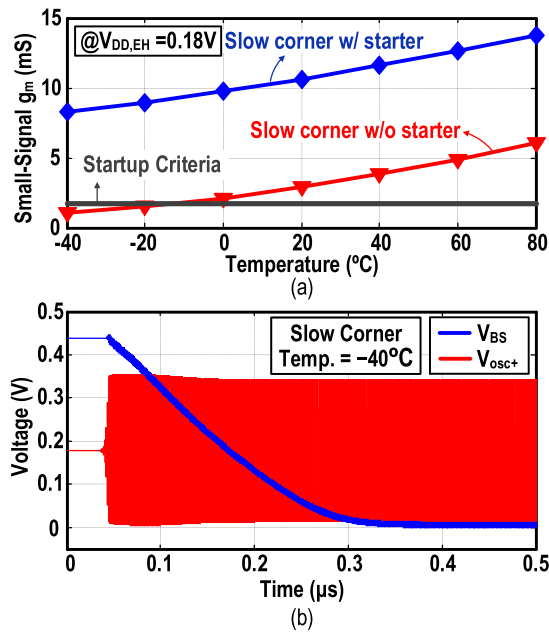


Fig. 7. Simulated (a) small-signal  $g_m$  of MD versus temperature at the slow corner and (b) voltage waveforms during startup under the slow corner and temperature of  $-40^{\circ}\text{C}$ . ( $V_{DD,EH} = 0.18\text{ V}$ ).

is added in parallel with the class-D core. A dynamic bias voltage  $V_{BS}$  ensures a robust startup.  $V_{BS}$  is generated by inverting  $V_{CP}$  which is the output of a passive CP continuously sensing the VCO outputs:  $V_{osc\pm}$ . When the VCO is starting up,  $V_{CP} \approx 0\text{ V}$ , and  $V_{BS}$  is pulled to  $V_{DD,INT}$  provided by CP<sub>2</sub>. During the startup, the class-C starter is biased at a voltage of  $\sim 0.45\text{ V}$  higher than the  $V_{TH}$  of MD. Thus, it can deliver a large negative transconductance in presence of PVT variations using  $M_C$  with a smaller transistor size:  $(W/L)_{M_C} = (W/L)_{M_D}/25$ . When oscillation has been built up, the large-signal transconductance of the class-D core is sufficient to sustain the oscillation, so that the class-C starter can be turned off to reduce the power consumption and prevent the phase noise degradation. This is done automatically since the passive CP would charge  $V_{CP}$  to  $V_{DD,EH} + V_{osc,pp}$ , which pulls  $V_{BS}$  to ground. As shown in Fig. 7(b), at  $T = -40^{\circ}\text{C}$  and slow corner, the VCO starts up within 45 ns and the average  $g_m$  ( $\sim 4.5\text{ mS}$ ) of  $M_D$  during stable oscillation well exceeds the startup criteria. The output swing slightly decreases by 19 mV after the class-C starter is completely turned off. At  $T = 27^{\circ}\text{C}$  and typical corner, the simulated startup time VCO is 25 ns. After the class-C starter is completely turned off, the VCO power is significantly reduced by  $2.3\times$  from 330 to 145  $\mu\text{W}$  while the phase noise at 2.5-MHz offset is improved by 3.3 dB. The simulated output swing is 0.35 to 0.63  $V_{pp}$  for  $V_{DD,EH} = 0.18\text{--}0.3\text{ V}$ , which is lower than  $3 \times V_{DD,EH}$  since the additional losses introduced by the switches become large when  $V_{DD,EH}$  is lower than the threshold voltage of  $M_D$  ( $\sim 0.3\text{ V}$ ).

To achieve low-power consumption, a large inductance value is preferable. Here a three-turn inductor has been chosen to realize an inductance of 4.49 nH while still keeping a high Q of  $\sim 20$ . Besides, for explicit power down and sleep-current

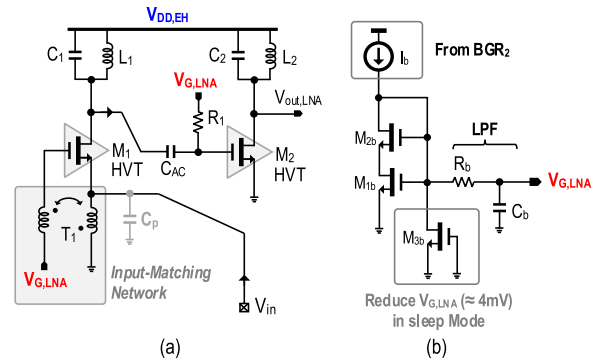


Fig. 8. (a) ULV two-stage power-gating LNA with on-chip input-impedance matching. (b) Its self-shutdown bias circuit in the sleep mode.

control, a tail switch is added for power gating. The control voltage of the switched-capacitor array for frequency tuning is provided by  $V_{DD,INT}$  from CP<sub>2</sub> drawing a neglectable dc current. The injection-lock port ( $V_{IL}$ ) is for RX testing, similar to [7].

## V. ULV RECEIVER (RX) PATH

The RX path mainly consists of an LNA, a passive I/Q generator, four passive mixers and four BB TIAs as detailed next.

### A. ULV Two-Stage Power-Gating LNA

As shown in Fig. 8(a), the single-ended single-transistor ( $M_1$ ) LNA features an on-chip transformer ( $T_1$ ) for input-impedance matching and passive gain boosting between  $M_1$ 's source and gate terminals [17]. Both the primary and secondary coils of  $T_1$  have an inductance of  $\sim 5.4\text{ nH}$ , and a low Q factor of  $\sim 5.6$ . They are reversely-coupled with a coupling factor of 0.86. From simulations at  $V_{DD,EH} = 0.18\text{ V}$ , the dc current of the LNA's first stage can be reduced from 2.1 mA (without  $T_1$ ) to 612  $\mu\text{A}$  (with  $T_1$ ) for a similar voltage gain and input-matching quality. ULV operation mainly challenges the large-signal linearity of the LNA. To balance the NF and linearity performances, the LNA's first stage is loaded with a low-Q LC tank ( $L_1C_1$ ) to provide a just-reasonable gain of  $\sim 14\text{ dB}$ . The LNA's second stage is designed to drive a capacitive load of 723 fF from the I/Q generator + passive mixers, and thus it only provides a 2-dB gain with a current consumption of 510  $\mu\text{A}$ . Both  $M_{1,2}$  are sized with a long-channel length (180 nm), and biased with an adequate overdrive ( $V_{GS} - V_{TH} \approx 110\text{ mV}$ ) to balance the linearity, gain and sleep current of the LNA [18]. The simulated IIP<sub>3</sub> and NF of the overall LNA is  $-17.4\text{ dBm}$ , and 9.84 dB, respectively, before considering the noise injected by the  $\mu\text{PM}$ . Moreover,  $M_{1,2}$  are HVT devices to suppress their sleep currents that simulate 0.55 nA in the sleep mode, against 0.23  $\mu\text{A}$  in low- $V_T$  devices. The LNA's blocker tolerability is limited at the output node of its second stage, which can be improved by introducing gain control while not affecting the input-impedance matching. It is preferred for BLE since the reference signal level is relaxed to  $-67\text{ dBm}$  under blocker performance measurement [19].

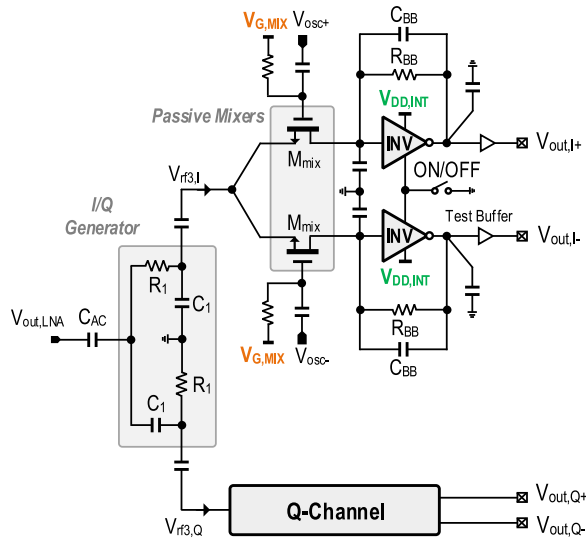


Fig. 9. RF path, passive I/Q generator, passive mixers, and BB TIAs.

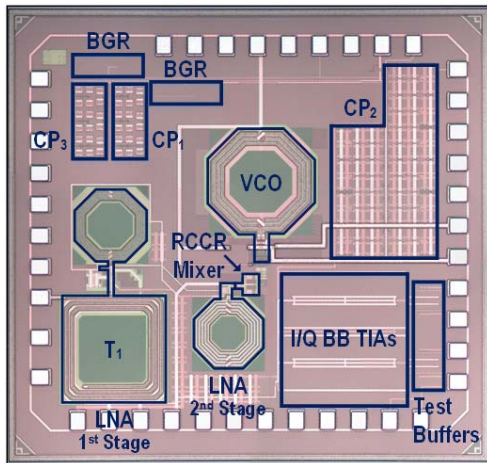


Fig. 10. Chip photograph of the ULV RX fabricated in 28-nm CMOS.

The current reference ( $I_b$ ) of the bias circuit is shown in Fig. 8(b). The current mirror has a supply voltage ( $V_{DD,PM1}$ ) of  $\sim 0.9$  V generated by CP<sub>1</sub>, thus it can provide a  $\sim 580$ -mV bias voltage ( $V_{G,LNA}$ ) for the HVT devices, while ensuring an adequate overdrive voltage. A low-pass filter,  $R_b$  (1 M $\Omega$ ) and  $C_b$  (40 pF), is added to prevent the  $\mu$ PM from injecting noise into the LNA.  $M_{1b,2b}$  are series connected to reduce the required  $I_b$  to 700 nA. To assess the robustness, we carried out 100-run Monte Carlo simulations on process variations. The dc current of the LNA varies  $< 3\%$ .

The bias circuit of the LNA has a self-shutdown mechanism. A 160/60 nm device,  $M_{3b}$ , is added with its gate tied to the ground as a  $\sim 60$ -M $\Omega$  MOS resistor. The resistance of  $M_{3b}$  is large compared to the diode-connected  $M_{1b}$  and  $M_{2b}$  at a high voltage, thus not affecting the generated  $V_{G,LNA}$  in the active mode. In the sleep mode, when the  $\mu$ PM is switched off, the impedance of the diode-connected  $M_{1b-2b}$  and BGR is large, thus the impedance of  $M_{3b}$  becomes relatively low pulling  $V_{G,LNA}$  to ground. From simulations,  $V_{G,LNA}$  is reduced from 160.6 to 3.3 mV via  $M_{3b}$ , reducing the leakage current from 9.13 to 0.55 nA at  $V_{DD,EH} = 0.18$  V.

### B. Passive I/Q Generator, Passive Mixers, and BB TIAs

The I/Q generator is an RC-CR network and the mixers are NMOS switches (Fig. 9). The I/Q generator realized in the RF path maximizes the LO swing at  $M_{mix}$  given by the VCO ( $V_{osc\pm} \approx 0.35V_{pp}$ ). With  $R_1 = 256 \Omega$  and  $C_1 = 260$  fF, the simulated insertion loss is  $< 7$  dB.  $R_1$  is implemented as two parallel-connected resistors to enhance the I/Q accuracy against process mismatches. We carried 100-run Monte Carlo simulations on process variations, showing a worst image-rejection ratio (IRR) of 25 dB, which is adequate for either zero-IF or low-IF reception for the BLE standard.

The passive mixers are biased at 450 mV via BGR<sub>2</sub> balancing the RX NF and conversion gain. The four passive mixers convert the I/Q RF signals into four BB I/Q differential signals for the BB TIAs.

Each BB TIA is an inverter-like amplifier with RC feedback ( $R$ : 23 k $\Omega$ ;  $C$ : 1.37 pF), consuming a simulated current of 25  $\mu$ A at a 0.46-V  $V_{DD,INT}$ . The TIA's transistors are relatively large (NMOS: 375/10  $\mu$ m and PMOS: 1020/10  $\mu$ m) to suppress their flicker noise for 0.5 MHz-IF downconversion. The TIA exhibits a simulated gain of 22.6 dB and bandwidth of 0.5 MHz. It shows a 22.5-dB rejection at 5-MHz offset for channel selection. The simulated input 1-dB gain compression of the TIA at 2-MHz offset is  $-7.8$  dBm. Two capacitors have been added at the input (4 pF) and output (20 pF) of the TIA to add two more real poles. They effectively suppress the  $2\times$ LO feedthrough component while aiding partially the channel selection. The common-mode noise injected by CP<sub>2</sub> is further suppressed at the BB TIA's differential outputs. To meet the BLE channel-selection specification, sub-0.5-mW BB filters similar to [5] or [22] should be added; the supply voltage can be provided by a CP similar to the architecture as shown in Fig. 3. With it, a low-power low-dynamic-range ADC is also expected for digitization.

## VI. MEASUREMENT RESULTS

The ULV RX prototyped in 28-nm CMOS (Fig. 10) occupies an active area of 1.65 mm<sup>2</sup>. The strict density rules are fulfilled. The measurements were conducted in a three-step approach: from the stand-alone  $\mu$ PM and VCO to the complete RX. The latter is aided by an external signal source to injection-lock the VCO, similar to [7], as there is no PLL in this prototype. We measured the startup characteristic of the  $\mu$ PM with the Tektronix MDO3024 Oscilloscope terminated with a 10-M $\Omega$  probe. The VCO and complete RX are measured with the Keysight 9030A PXA Signal Analyzer. The I/Q differential BB outputs are converted to single-ended via off-chip transformers crucial here to reject the common-mode noises.  $V_{DD,EH}$  is given by a typical power supply sweeping from 0.18 to 0.3 V to balance the overall performances.

### A. Stand-Alone $\mu$ PM

Fig. 11(a) plots the outputs of the  $\mu$ PM at  $V_{DD,EH} = 0.18$  V with an external enable signal (EN, in Fig. 2). The startup time is  $\sim 200 \mu$ s that can be overlapped with the fast startup time ( $\sim 50$ – $400 \mu$ s) of the state-of-the-art BLE crystal

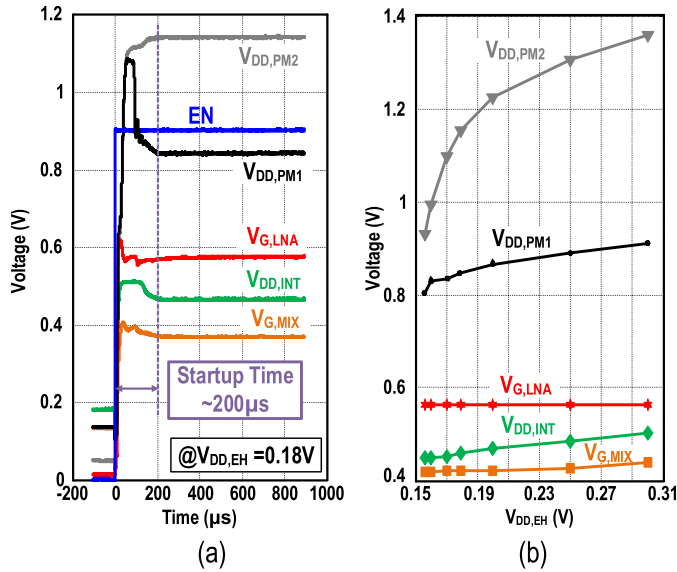


Fig. 11. Measured (a) startup transients of the  $\mu$ PM and (b) outputs against  $V_{DD,EH}$  variation.

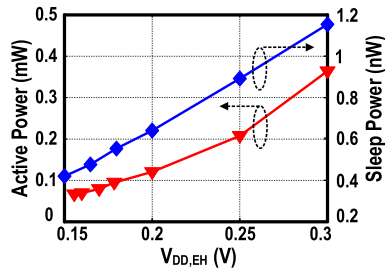


Fig. 12. Measured power consumption and sleep power of the  $\mu$ PM against  $V_{DD,EH}$  variation.

oscillator [20], [21]. Thus, the agility of the RX in launching a connection should not be affected. The voltages ramp up rapidly in  $\sim 50 \mu$ s while they take  $\sim 150 \mu$ s to stabilize. Thus, the startup time is dominated by the feedback control loop in CP<sub>1,2</sub>. Fig. 11(b) shows the voltage variation over  $V_{DD,EH}$  from 0.156 to 0.3 V. The variations of  $V_{G,LNA}$  and  $V_{DD,INT}$  are controlled to be 0.18% and 12%, respectively, saving the excessive power.  $V_{DD,PM1}$  and  $V_{DD,INT}$  increase with  $V_{ref,PM}$  mainly due to the increased voltage drop on the tail switch  $M_1$  (see Fig. 2) at a high  $V_{DD,EH}$ .

Fig. 12 shows the power consumption and leakage power of the  $\mu$ PM. Comparing Fig. 12 with Fig. 5(b), the power consumption goes up along with  $V_{DD,EH}$  which is mainly due to the free-running CP<sub>3</sub>. The power of BTRO in CP<sub>3</sub> also raises significantly with  $V_{DD,EH}$ , while the leakage power is nearly proportional to  $V_{DD,EH}$ .

### B. Stand-Alone VCO

Fig. 13(a)–(c) summarizes the phase noises of the free-running VCO at 2.3 and 2.6 GHz under different  $V_{DD,EH}$ . The worst phase noise is  $-113$  dBc/Hz at 2.5-MHz offset at the 2.3 GHz [Fig. 13(c)], still fulfilling the BLE standard. The VCO output power, including the loss of the test buffer [Fig. 13(d)] increases from  $-19$  to  $-13$  dBm when  $V_{DD,EH}$  goes up from 0.18 to 0.3 V. The frequency tuning range is

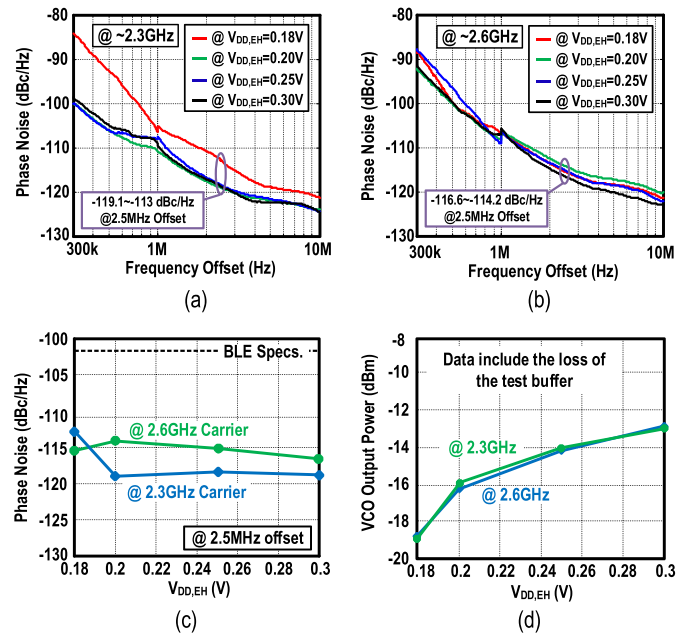


Fig. 13. Measured performances of the class-D VCO. (a) and (b) Phase noises at  $\sim 2.3$  GHz and  $\sim 2.6$  GHz. (c) Phase noise and (d) output power against  $V_{DD,EH}$  variation.

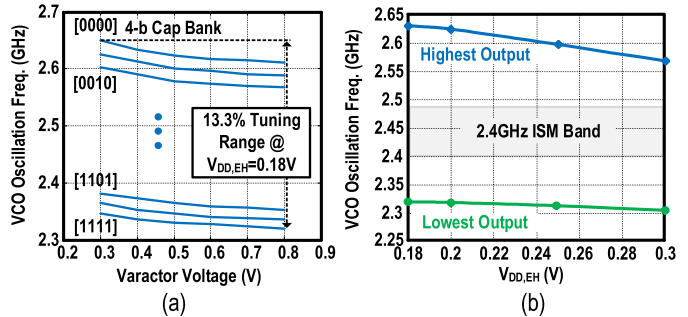


Fig. 14. Measured (a) frequency tuning range of the class-D VCO and (b) frequency pulling against  $V_{DD,EH}$  variation.

13.3% [Fig. 14(a)], and Fig. 14(b) plots the supply pulling versus  $V_{DD,EH}$ . On the other hand, Fig. 15 exhibits the active and sleep powers versus  $V_{DD,EH}$ . The lowest active power is  $153 \mu$ W and the leakage power is  $0.45$  nW, at  $V_{DD,EH} = 0.18$  V.

### C. Complete RX

The VCO is injection locked to an external RF source for a stable RX NF measurement [7]. It is achieved by injecting a  $2 \times$ LO frequency signal at the common-mode node  $V_{IL}$ . The input-impedance matching of the LNA [Fig. 16(a)] shows a 100-MHz matching bandwidth with small variation as  $V_{DD,EH}$  changes. Yet, the matching bandwidth is upshifted by  $\sim 50$  MHz from the 2.4-GHz ISM band, which is likely due to the inaccuracy of the transformer modeling. The RF-to-BB quadrature gain is 34.5 dB at 0.18 V, and up to 41.3 dB at 0.3 V [Fig. 16(b)]. The RF-to-BB gain increases mainly due to the enlarged  $V_{DD,INT}$  of the BB TIAs from CP<sub>2</sub>, since the TIAs are self-biased.

Fig. 16(c) illustrates the double sideband (DSB) NF and out-of-band IIP<sub>3</sub>. A DSB NF of 11.3 dB is achieved at 1 MHz IF at  $V_{DD,EH} = 0.18$  V. It is improved to 8.8 dB when

TABLE I  
 COMPARISON WITH THE STATE-OF-THE-ART ULP RXS (PLL IS NOT INCLUDED)

	This Work		JSSC'15 [5] [A. Selvakumar, et al.]	JSSC'13 [7] [F. Zhang, et al.]	JSSC'14 [6] [Z. Lin, et al.]
Applications	2.4GHz BLE		2.4GHz BLE	2.4GHz Non-Standard	2.4GHz ZigBee
Key Architecture & Circuit Techniques	Power-Gating LNA + ULV Class-D VCO + Passive I/Q Gen. + Micro-Power Manager		Current-Reuse Quadrature-LNA-Mixer-VCO Cell	Transformer-Coupling LNA and VCO + IF N-Path Filter	Current Reuse RF-to-BB Cell + VCO & DIV-by-4
External Matching	Zero		1 inductor + 1 cap.	1 inductor + 2 caps.	zero
Supply Voltage (V)	0.18	0.3	0.8	0.3	0.6 & 1.2
Active Power ( $\mu$ W)	382	1305	600 <sup>1</sup>	1600	2700 <sup>1</sup>
Sleep Power (nW)	1.33	3.32	N/A	N/A	N/A
NF (dB)	11.3	8.8	15.1 to 15.8	6.1	9
VCO Phase Noise (dBc/Hz) @ Offset	-113 to -115.5 @ 2.5 MHz	-116.6 to -118.9 @ 2.5 MHz	-109 @ 2.5 MHz	-112.8 @ 1 MHz	N/A
	[BLE spec: -102 @ 2.5 MHz] <sup>2</sup>				
Out-of-Band IIP3 (dBm)	-12.5	+4.8	-15.8 to -16.8	-21.5	-6
	[BLE Spec: -30] <sup>2</sup>				
IRR (dB)	26.2	25.1	30.5 to 37.3	N/A (no I/Q)	28
	[BLE Spec: 21] <sup>2</sup>				
Voltage Gain (dB)	34.5	41.3	55.5 to 56.1	83	55
BB Style	With I/Q		With I/Q	Without I/Q	With I/Q
BB Filtering	3 real poles <sup>3</sup>		2 complex poles	2 N-path filters	3 complex poles
Active Area (mm <sup>2</sup> )	1.65		0.25	~1.7	0.26
Technology	28nm CMOS		130nm CMOS	65nm CMOS	65nm CMOS

<sup>1</sup> [5]-[6] have not included the loss, power and area of the power-management units if using a sub-0.5V energy-harvesting source.

<sup>2</sup> BLE specifications from [5]. <sup>3</sup> Partial channel-selection filtering.

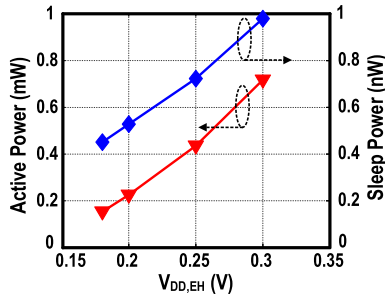


Fig. 15. Measured power consumption and sleep power of the class-D VCO against  $V_{DD,EH}$  variation.

$V_{DD,EH} = 0.3$  V. Limited by the bandwidth of the BB TIAs, the DSB NF at 1-MHz IF is higher than that at 0.4 MHz. An IF of 0.5 MHz is expected to achieve low NF and avoid signal distortion. Without differential combining, the ripple injection from CP<sub>2</sub> can degrade the DSB NF by 5–6 dB at 0.1–0.8-MHz IF. With a two-tone test at 3- and 5-MHz offsets from the LO frequency, the RX shows a reasonable IIP3 of –12.5 dBm [Fig. 16(d)] even at  $V_{DD,EH} = 0.18$  V, due to the adequate and stable bias voltages generated by the  $\mu$ PM. The measured 5-MHz in-band  $P_{1\text{ dB}}$  blocker power of the LNA is –27.5 dBm [Fig. 16(e)]. The NF against the in-band (2.5 GHz + 3 MHz) and out-of-band (1.9 GHz) blocker power is shown in Fig. 16(f). The NF is degraded to 20 dB at –26 dBm (2 dBm) for the in-band (out-of-band) blocker. The IRR of the RX is >25.1 dB.

#### D. Power Breakdown in the Active/Sleep Mode

Fig. 17 outlines the total active and sleep power at different  $V_{DD,EH}$ . The total power consumption at  $V_{DD,EH} = 0.18$  V is 382  $\mu$ W, where 75% of current is drawn directly from  $V_{DD,EH}$  and only 25% of the current passing through the  $\mu$ PM. At  $V_{DD,EH} = 0.3$  V, the power consumption goes up to 1.3 mW, with main contribution from the Class-D VCO since its gate bias is tied directly to  $V_{DD,EH}$ . At  $V_{DD,EH} = 0.18$  V, the leakage power is as low as 1.33 nW, thanks to the ULV operation and the use of long-channel HVT devices for the LNA and other power-gating switches.

#### E. Performance Benchmark

Comparing with the state-of-the-art ULP RXs in Table I [5]–[7], this paper, aided by a  $\mu$ PM, succeeds in operating against a deeply low and uncertain supply voltage, while consuming low active and sleep power. No external components are entailed. These are all crucial parameters for low-cost energy-harvesting IoT applications. Note that [5]–[6] have not included the loss, power and area of their power-management units if using a sub-0.5-V energy-harvesting source. The power consumption here is optimized at 0.18 V, but is sub-optimized at 0.3 V due to the excessive VCO power. I/Q demodulation is supported for the BLE, while [7] does not. The main expense of this ULV ULP RX is the active area (1.65 mm<sup>2</sup>), which is dominated by the utilization of three coils in the LNA and the fully integrated  $\mu$ PM.

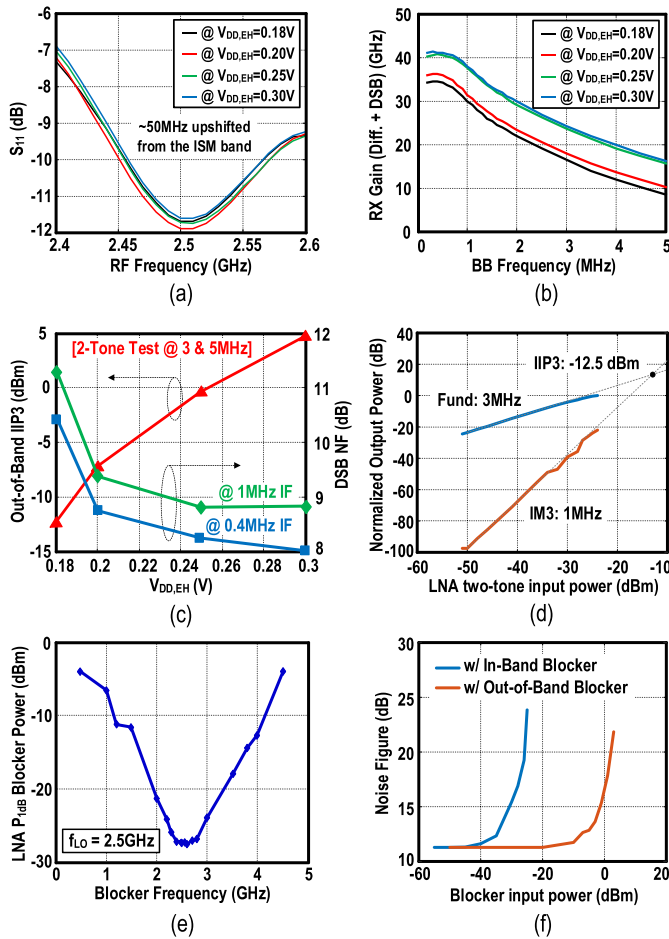


Fig. 16. Measured RX (a)  $S_{11}$ , (b) RF-to-BB gain against  $V_{DD,EH}$ , (c) NF and out-of-band IIP3 against  $V_{DD,EH}$ , (d) in-band IIP3 profile at  $V_{DD,EH} = 0.18$  V, (e) blocker  $P_{1dB}$  against blocker frequency, and (f) NF against blocker power at  $V_{DD,EH} = 0.18$  V.

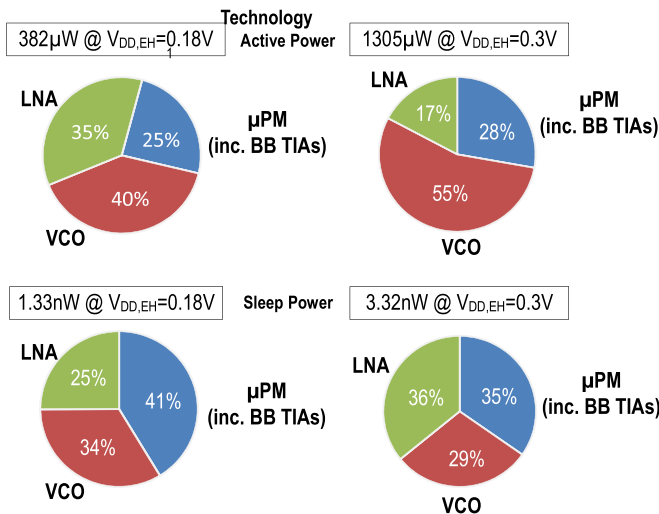


Fig. 17. Breakdown of active and sleep power at  $V_{DD,EH} = 0.18$  and  $0.3$  V.

Note that the PLL is not included in [5]–[7] and this paper. A 0.2-V analog type-I PLL with VCO for BLE has been recently demonstrated in [23], with a total power consumption of  $\sim 0.7$  mW. We also acknowledge that although this paper has managed to lower the power consumption, it has a higher NF than the recent BLE RXs [24], [25].

## VII. CONCLUSION

An ULV RX front-end-aided by an on-chip  $\mu$ PM has been presented. It aims at direct powering by a sub-0.5-V energy-harvesting source without further power regulation. The circuit techniques are: 1) an  $\mu$ PM to deliver the internal supply voltages and biases unlimited by the energy-harvesting voltage; 2) an ULV 3-coil two-stage LNA with an on-chip input transformer to enhance the NF and gain, and power-gating to suppress the sleep power; and 3) an ULV Class-D VCO assisted by a Class-C starter to ensure robust and fast startup. Fabricated in 28-nm CMOS, the RX prototype achieves low active power (382  $\mu$ W) and sleep power (1.33 nW) down to 0.18 V, while being compliant with the BLE standard.

## REFERENCES

- [1] Bluetooth. (2013). *Bluetooth Specification Version 4.1*. [Online]. Available: <http://www.bluetooth.com>
- [2] T. Torfs *et al.*, “Wearable autonomous wireless electro-encephalography system fully powered by human body heat,” in *Proc. IEEE Sensors*, Oct. 2008, pp. 1269–1272.
- [3] S. Bandyopadhyay and A. P. Chandrakasan, “Platform architecture for solar, thermal, and vibration energy combining with MPPT and single inductor,” *IEEE J. Solid-State Circuits*, vol. 47, no. 9, pp. 2199–2215, Sep. 2012.
- [4] J. Kim, P. K. T. Mok, and C. Kim, “A 0.15 V input energy harvesting charge pump with dynamic body biasing and adaptive dead-time for efficiency improvement,” *IEEE J. Solid-State Circuits*, vol. 50, no. 2, pp. 414–425, Feb. 2015.
- [5] A. Selvakumar, M. Zargham, and A. Liscidini, “Sub-mW current reuse receiver front-end for wireless sensor network applications,” *IEEE J. Solid-State Circuits*, vol. 50, no. 12, pp. 2965–2974, Dec. 2015.
- [6] Z. Lin, P.-I. Mak, and R. P. Martins, “A 2.4 GHz ZigBee receiver exploiting an RF-to-BB-current-reuse Blixer + hybrid filter topology in 65 nm CMOS,” *IEEE J. Solid-State Circuits*, vol. 49, no. 6, pp. 1333–1344, Jun. 2014.
- [7] F. Zhang, Y. Miyahara, and B. P. Otis, “Design of a 300-mV 2.4-GHz receiver using transformer-coupled techniques,” *IEEE J. Solid-State Circuits*, vol. 48, no. 12, pp. 3190–3205, Dec. 2013.
- [8] A. Paidimarri, N. Ickes, and A. P. Chandrakasan, “A +10 dBm BLE transmitter with sub-400 pW leakage for ultra-low duty cycles,” *IEEE J. Solid-State Circuits*, vol. 51, no. 6, pp. 1331–1346, Jun. 2016.
- [9] W.-H. Yu, H. Yi, P.-I. Mak, J. Yin, and R. P. Martins, “A 0.18 V 382  $\mu$ W Bluetooth low-energy (BLE) receiver with 1.33 nW sleep power for energy-harvesting applications in 28 nm CMOS,” in *IEEE Int. Solid-State Circuits Conf. (ISSCC) Dig. Tech. Papers*, Feb. 2017, pp. 414–415.
- [10] Q. Lv *et al.*, “Solid-state thin-film supercapacitors with ultra-fast charge/discharge based on N-doped-carbon-tubes/au-nanoparticles-doped-MnO<sub>2</sub> nanocomposites,” *ACS Nano Lett.*, vol. 16, no. 1, pp. 40–47, Nov. 2015.
- [11] L. Fanori and P. Andreani, “Class-D CMOS Oscillators,” *IEEE J. Solid-State Circuits*, vol. 48, no. 12, pp. 3105–3119, Dec. 2013.
- [12] Y. Ho, Y.-S. Yang, C. Chang, and C. Su, “A near-threshold 480 MHz 78  $\mu$ W all-digital PLL with a bootstrapped DCO,” *IEEE J. Solid-State Circuits*, vol. 48, no. 11, pp. 2805–2814, Nov. 2013.
- [13] H. Yi, J. Yin, P.-I. Mak, and R. P. Martins, “A 0.032-mm<sup>2</sup> 0.15-V three-stage charge-pump scheme using a differential bootstrapped ring-VCO for energy-harvesting applications,” *IEEE Trans. Circuits Syst. II, Exp. Briefs*, vol. 65, no. 2, pp. 146–150, Feb. 2018.
- [14] H.-P. Le, S. R. Sanders, and E. Alon, “Design techniques for fully integrated switched-capacitor DC–DC converters,” *IEEE J. Solid-State Circuits*, vol. 46, no. 9, pp. 2120–2131, Sep. 2011.
- [15] T. Van Bruessegem and M. Steyaert, “A 82% efficiency 0.5% ripple 16-phase fully integrated capacitive voltage doubler,” in *IEEE Symp. VLSI Circuits Dig.*, Jun. 2009, pp. 198–199.
- [16] D. Ma and F. Luo, “Robust multiple-phase switched-capacitor DC–DC power converter with digital interleaving regulation,” *IEEE Trans. Very Large Scale Integr. (VLSI) Syst.*, vol. 16, no. 6, pp. 611–619, Jun. 2008.
- [17] X. Li, S. Shekhar, and D. J. Allstot, “ $G_m$ -boosted common-gate LNA and differential Colpitts VCO/QVCO in 0.18- $\mu$ m CMOS,” *IEEE J. Solid-State Circuits*, vol. 40, no. 12, pp. 2609–2619, Dec. 2005.

- [18] T. Soorapanth and T. H. Lee, "RF linearity of short-channel MOSFETs," in *Proc. Int. Workshop Design Mixed-Mode Integr. Circuits Appl.*, Jul. 1997, pp. 81–84.
- [19] J. Prummel *et al.*, "A 10 mW Bluetooth low-energy transceiver with on-chip matching," *IEEE J. Solid-State Circuits*, vol. 50, no. 12, pp. 3077–3088, Dec. 2015.
- [20] D. Griffith, J. Murdock, and P. T. Røine, "A 24 MHz crystal oscillator with robust fast start-up using dithered injection," in *IEEE Int. Solid-State Circuits Conf. (ISSCC) Dig. Tech. Papers*, Jan./Feb. 2016, pp. 104–105.
- [21] Y. I. Kwon, S.-G. Park, T.-J. Park, K.-S. Cho, and H.-Y. Lee, "An ultra low-power CMOS transceiver using various low-power techniques for LR-WPAN applications," *IEEE Trans. Circuits Syst. I, Reg. Papers*, vol. 59, no. 2, pp. 324–336, Feb. 2012.
- [22] Y.-H. Liu *et al.*, "A 3.7 mW-RX 4.4 mW-TX fully integrated Bluetooth Low-Energy/IEEE802.15.4/proprietary SoC with an ADPLL-based fast frequency offset compensation in 40 nm CMOS," in *IEEE Int. Solid-State Circuits Conf. (ISSCC) Dig. Tech. Papers*, Feb. 2015, pp. 236–237.
- [23] J. Yin, S. Yang, H. Yi, W.-H. Yu, P.-I. Mak, and R. P. Martins, "A 0.2 V energy-harvesting BLE transmitter with a micropower manager achieving 25% system efficiency at 0dBm output and 5.2 nW sleep power in 28 nm CMOS," in *IEEE Int. Solid-State Circuits Conf. (ISSCC) Dig. Tech. Papers*, Feb. 2018, pp. 450–451.
- [24] T. Sano *et al.*, "A 6.3 mW BLE transceiver embedded RX image-rejection filter and TX harmonic-suppression filter reusing on-chip matching network," in *IEEE Int. Solid-State Circuits Conf. (ISSCC) Dig. Tech. Papers*, Feb. 2015, pp. 240–241.
- [25] K. W. Kuo *et al.*, "A Bluetooth low-energy transceiver with 3.7-mW all-digital transmitter, 2.75-mW High-IF discrete-time receiver, and TX/RX switchable on-chip matching network," *IEEE J. Solid-State Circuits*, vol. 52, no. 4, pp. 1144–1162, Apr. 2017.



**Haidong Yi** (S'16) received the B.Sc. degree in electronic science and technology from Henan University, Kaifeng, China, and the M.Eng. degree in microelectronics from Fudan University, Shanghai, China, in 2012 and 2015, respectively. He is currently pursuing the Ph.D. degree in electronic and computer engineering with the University of Macau, Macao, China, with focusing on the ultra-low-voltage low-power analog and RF circuit techniques.



**Wei-Han Yu** (S'09) received the B.Sc. and M.Sc. degrees in electrical and electronics engineering from the University of Macau (UM), Macao, China, in 2010 and 2012, respectively, and the Ph.D. degree from the State-Key Laboratory of Analog and Mixed-Signal VLSI and Faculty of Science and Technology, Department of Electronic and Computer Engineering, UM, in 2018.

He is currently a Post-Doctoral Researcher at UM. His current research interests include RF and mm-wave transmitter, power amplifier, digital predistortion, and EM modeling for next-generation mobile communications.

Dr. Yu was a recipient the IEEE ISSCC STGA Award and the FDCT S&T Postgraduate Student Award in 2016, and the IEEE SSCS Predoctoral Achievement Award in 2018.



**Pui-In Mak** (S'00–M'08–SM'11) received the Ph.D. degree from the University of Macau (UM), Macao, China, in 2006.

He is currently a Full Professor with the Faculty of Science and Technology, Department of Electronic and Computer Engineering, UM, and an Associate Director (Research) with the State Key Laboratory of Analog and Mixed-Signal VLSI, UM. His current research interests include analog and radio-frequency (RF) circuits and systems for wireless and multidisciplinary innovations.

Prof. Mak co-received the DAC/ISSCC Student Paper Award 2005, the CASS Outstanding Young Author Award 2010, the National Scientific and Technological Progress Award 2011, the Best Associate Editor of IEEE Transactions on Circuits and Systems II 2012 and 2013, the A-SSCC Distinguished Design Award 2015, and the ISSCC Silkroad Award 2016. In 2005, he was decorated with the Honorary Title of Value for scientific merits

by the Macau Government. He was an Editorial Board Member of IEEE Press from 2014 to 2016, a member of the Board-of-Governors of IEEE Circuits and Systems Society from 2009 to 2011, a Senior Editor of the IEEE Journal on Emerging and Selected Topics in Circuits and Systems from 2014 to 2015, and an Associate Editor of the IEEE Transactions on Circuits and Systems I from 2010 to 2011 and 2014 to 2015 and II 2010 to 2013. He has been an Associate Editor of the IEEE JOURNAL OF SOLID-STATE CIRCUITS and the IEEE Solid-State Circuits Letters since 2017. He was the TPC Vice Co-Chair of ASP-DAC in 2016, a TPC Member of A-SSCC from 2013 to 2016, ESSCIRC from 2016 to 2017. He has been a TPC Member of ISSCC since 2016. He was a Distinguished Lecturer of the IEEE Circuits and Systems Society from 2014 to 2015 and is currently the IEEE Solid-State Circuits Society. He is currently the Chair of the Distinguished Lecturer Program of IEEE Circuits and Systems Society.



**Jun Yin** (M'14) received the B.Sc. and M.Sc. degrees in microelectronics from Peking University, Beijing, China, in 2004 and 2007, respectively, and the Ph.D. degree in electronic and computer engineering from the Hong Kong University of Science and Technology, Hong Kong, in 2013.

He is currently an Assistant Professor with the State Key Laboratory of Analog and Mixed-Signal VLSI, University of Macau, Macao, China. His current research interests include CMOS RF integrated circuits for wireless communication and wireless sensing systems, specializing in the frequency generation and synthesis circuits including oscillators and phase-locked loops.



**Rui P. Martins** (M'88–SM'99–F'08) was born in 1957. He received the bachelor's, master's, and Ph.D. degrees, as well as the Habilitation for Full-Professor in electrical engineering and computers from the Department of Electrical and Computer Engineering, Instituto Superior Técnico (IST), TU of Lisbon, Lisbon, Portugal, in 1980, 1985, 1992, and 2001, respectively.

He has been with the Department of Electrical and Computer Engineering, IST, since 1980. Since 2013, he has been with the Faculty of Science and Technology (FST), Department of Electrical and Computer Engineering, University of Macau (UM), Macao, China, as a Chair-Professor. In FST, he was the Dean of the Faculty from 1994 to 1997. He has been a Vice-Rector of the UM since 1997. From 2008, after the reform of the UM Charter, he was nominated after open international recruitment, and reappointed in 2013, as a Vice-Rector (Research) until 2018. Within the scope of his teaching and research activities, he has taught 21 bachelor and master courses, and in UM, has supervised (or co-supervised) 19 Ph.D. theses and 21 Master theses. He was a Co-Founder of Chipidea Microelectronics (Macao) (now Synopsys) from 2001 to 2002, and the Founding Director of the Analog and Mixed-Signal VLSI Research Laboratory of UM, and the State Key Laboratory of China (the first in Engineering in Macao). He has co-authored six books and nine book chapters, and 111 papers in scientific journals and 266 papers in conference proceedings, as well as other 60 academic works. He holds 16 US Patents and 2 Taiwan Patents.

Dr. Martins was a Nominations Committee Member of the IEEE CASS in 2016 and is currently the Chair of the IEEE Fellow Evaluation Committee of IEEE CASS, class of 2018. He was a member of the IEEE CASS Fellow Evaluation Committee from 2013 to 2014, and CAS Society representative in the Nominating Committee, for the election in 2014, of the Division I (CASS/EDS/SSCS)—Director of the IEEE. He was a recipient of the Medal of Professional Merit from Macao Government (Portuguese Administration) in 1999, and the Honorary Title of Value from Macao SAR Government (Chinese Administration) in 2001. He was the Founding Chairman of the IEEE Macau Section from 2003 to 2005 and the IEEE Macau Joint-Chapter on Circuits and Systems (CAS)/Communications from 2005 to 2008 [2009 World Chapter of the Year of the IEEE CAS Society (CASS)]. He was the General Chair of the 2008 IEEE Asia-Pacific Conference on CAS—APCCAS'2008, and the Vice-President for Region 10 (Asia, Australia, and the Pacific) of the IEEE CASS from 2009 to 2011. Since then, he was the Vice-President (World) Regional Activities and Membership of the IEEE CASS from 2012 to 2013, and an Associate Editor of the IEEE TRANSACTIONS ON CAS II: EXPRESS BRIEFS from 2010 to 2013, nominated the Best Associate Editor of T-CAS II from 2012 to 2013. He was the General Chair of the ACM/IEEE Asia South Pacific Design Automation Conference—ASP-DAC'2016. In 2010, he was elected, unanimously, as a Corresponding Member of the Portuguese Academy of Sciences, Lisbon, being the only Portuguese Academician living in Asia.